



A novel nanoporous α -C₃N₄ photocatalyst with superior high visible light activity



Guosheng Wu, Sapanbir S. Thind, Jiali Wen, Kai Yan, Aicheng Chen*

Department of Chemistry, Lakehead University, 955 Oliver Road, Thunder Bay, Ontario P7B 5E1, Canada

ARTICLE INFO

Article history:

Received 2 April 2013

Received in revised form 26 May 2013

Accepted 29 May 2013

Available online 6 June 2013

Keywords:

Nanoporous photocatalyst

α -C₃N₄

Visible light activity

Solution combustion reaction

ABSTRACT

Here we report on a novel metal-free α -C₃N₄ nanoporous photocatalyst for promising energy and environmental applications. The nanoporous material was synthesized via a facile solution combustion reaction utilizing urea as both the precursor and fuel for the first time. Characterization results derived from N₂ adsorption, X-ray diffraction and transmission electron microscope revealed that the synthesized photocatalyst exhibited a nanoporous structure with a high degree of crystallinity. UV–vis absorption and high resolution valence band X-ray photoelectron spectroscopic analysis showed that the band gap energy of the α -C₃N₄ nanoporous photocatalyst was \sim 2.76 eV with a valence band maxima located at 1.71 eV, which constitutes an ideal position that is suitable for water splitting. Our study demonstrates that the α -C₃N₄ photocatalyst has high stability and exceptional activity for the generation of hydrogen and for the degradation of organic pollutants under visible light irradiation.

© 2013 Elsevier B.V. All rights reserved.

1. Introduction

Secure and clean energy production and the protection of the environment are two of the most critical issues facing the world today. Fossil fuels have been exploited as a primary energy source for over one hundred years. However, supplies of raw oil and natural gas are limited. In addition, greenhouse gas emissions and other pollutants generated through the combustion of these fossil fuels result in serious environmental problems. Therefore, the prospect of a clean, reliable and sustainable energy supply has attracted increasing attention over the last several decades. Due to its high energy capacity and environmental compatibility, hydrogen has emerged as one of the most promising fuels for meeting future global energy demands [1,2]. Currently, industry produces H₂ mainly from the steam–methane reforming (SMR) of natural gas [3]. Ironically, however, the SMR process generates enormous amounts of CO₂ (5 kg CO₂/kg H₂), resulting in serious environmental consequences. It is thus crucial to evolve clean and sustainable methods for the production of H₂.

The photocatalytic generation of H₂ from water splitting utilizing solar energy is one of the most promising approaches [4,5]. Highly efficient and stable photocatalysts are essential to this process [6–9]. To achieve water splitting, the conduction band (CB) of a photocatalyst must be located at a lower electrode potential than the reduction potential of H⁺/H₂ (0.0 V vs. NHE at pH 0), while the

valence band (VB) must be positioned more positively than the oxidation potential of H₂O/O₂ (1.23 V vs. NHE) [4]. To date, most of the photocatalysts utilized in the generation of H₂ have been comprised of transition metal oxides (e.g., TiO₂, ZnO, WO₃), doped transition metal oxides and other classes of semiconductors, such as ZnS and CdS [10–15]. The major drawbacks inherent to these transition metal oxides, in terms of water splitting, are their large band gap energy and inappropriate band gap positions. For instance, TiO₂ has been intensively studied for photocatalytic water splitting due to its high efficiency and photostability; however, its band gap is too large (e.g., 3.2 eV for anatase TiO₂). Thus, UV light is required to activate TiO₂ in the generation of electron–hole pairs. In the solar spectrum, visible light accounts for \sim 45% of the energy that cannot be harvested by pristine TiO₂ [16]. In order to shift the absorption edge of these transition metal oxides to the visible light region, a number of approaches have been explored. The most common techniques have involved doping with metals or non-metal elements such as Fe, Cr, C, W, N and S [16–24], the formation of semiconductor composites [7,25], and the enhancement of photonic sensitization via the integration of dyes or quantum dots [26–29]. Although doping with impurity atoms may narrow the band gap energy of metal oxides, absorption edge shifting to longer wavelengths does not guarantee that high photocatalytic activity will be obtained [30]. This is due to the fact that the doping process may cause defects or induce lattice strain within crystalline domains, which serve as recombination centers, thus lowering their response to light. Semiconductor composites are comprised of both high and low band gap photocatalysts to exploit visible light due to electron transfer between the two. There remain, however, issues associated

* Corresponding author. Tel.: +1 807 3438318; fax: +1 807 3467775.

E-mail address: aicheng.chen@lakeheadu.ca (A. Chen).

with these types of materials as well. It is a challenge to prepare homogeneous solid solutions and to obtain appropriate valence and conduction energy level positional alignments between different semiconducting compounds. In addition, there remain significant challenges to overcome in the design and fabrication of new materials with high stability and efficiency for the generation of H_2 via water splitting.

Recently, polymeric materials such as graphitic carbon nitride ($g\text{-C}_3\text{N}_4$) have been synthesized and studied as an emerging photocatalyst [31–36]. The $g\text{-C}_3\text{N}_4$ compound has been prepared via the pyrolysis of nitrogen-rich precursors through bulk reaction or poly-condensation. In this study, for the first time, we have synthesized a novel metal-free nanoporous photocatalyst ($\alpha\text{-C}_3\text{N}_4$) with high stability and photocatalytic efficiency using a facile solution combustion reaction. The band gap energy, valence and conduction band positions of the new as-obtained photocatalyst were found to be ideal for water splitting. Our studies have shown that this nanomaterial possesses considerable H_2 generation and high organic pollutant degradation efficiencies under both all arc and visible light irradiation, superior than that of $g\text{-C}_3\text{N}_4$.

2. Experimental methods

2.1. Fabrication of the metal-free nanoporous photocatalysts

Urea (99.99%) was employed in this work to synthesize the nanoporous $\alpha\text{-C}_3\text{N}_4$ photocatalyst. In a typical condition, 15 g urea was added to 20 ml of distilled water; the solution was stirred for 30 min until all of the urea was dissolved, and then heated to 400 °C.

The solid products were heated further at 450 °C over different time periods, which varied from one to three hours. The $g\text{-C}_3\text{N}_4$ photocatalyst, which was employed for comparison in this study, was prepared by annealing melamine. The reaction proceeded in a covered alumina crucible that provided a semi-enclosed environment to prevent the sublimation of the precursor. In a typical experiment, 5 g of melamine was introduced into the crucible, which was heated to 500 °C in a muffle furnace at a heating rate of 15 °C/min and sustained for 4 h. Subsequently, the temperature was raised to 520 °C and sustained for 2 h, after which the crucible was cooled naturally to room temperature.

2.2. Characterization of the nanostructured photocatalysts

The as-synthesized nanoporous materials were characterized by X-ray diffraction (XRD, Philips PW 1050-3710 Diffractometer with Cu $K\alpha$ radiation, 40 kV, 30 mA) and a transmission electron microscope (TEM, JEOL 2010 microscope). The surface composition was further investigated using X-ray photoelectron spectroscopy (XPS, Omicron EA-125 energy analyzer and a multichannel detector) using a monochromatic Mg $K\alpha$ X-ray source ($h\nu = 1253.6$ eV). All binding energies reported in this work were corrected using the C 1s peak at 284.5 eV as an internal standard. UV–vis spectra were collected using a Varian Cary 5E. Time-of-flight secondary ion mass spectroscopy (ToF-SIMS) was recorded using an ION-TOF IV system 5-100 (ION-TOF, Muenster Germany). Analysis sites were constrained to 500 $\mu\text{m} \times 500 \mu\text{m}$, while maintaining a primary ion dose density of 10^{12} ions/ cm^2 or lower, to ensure static SIMS. Thermal analysis experiments were carried out utilizing a NETZSCH TG

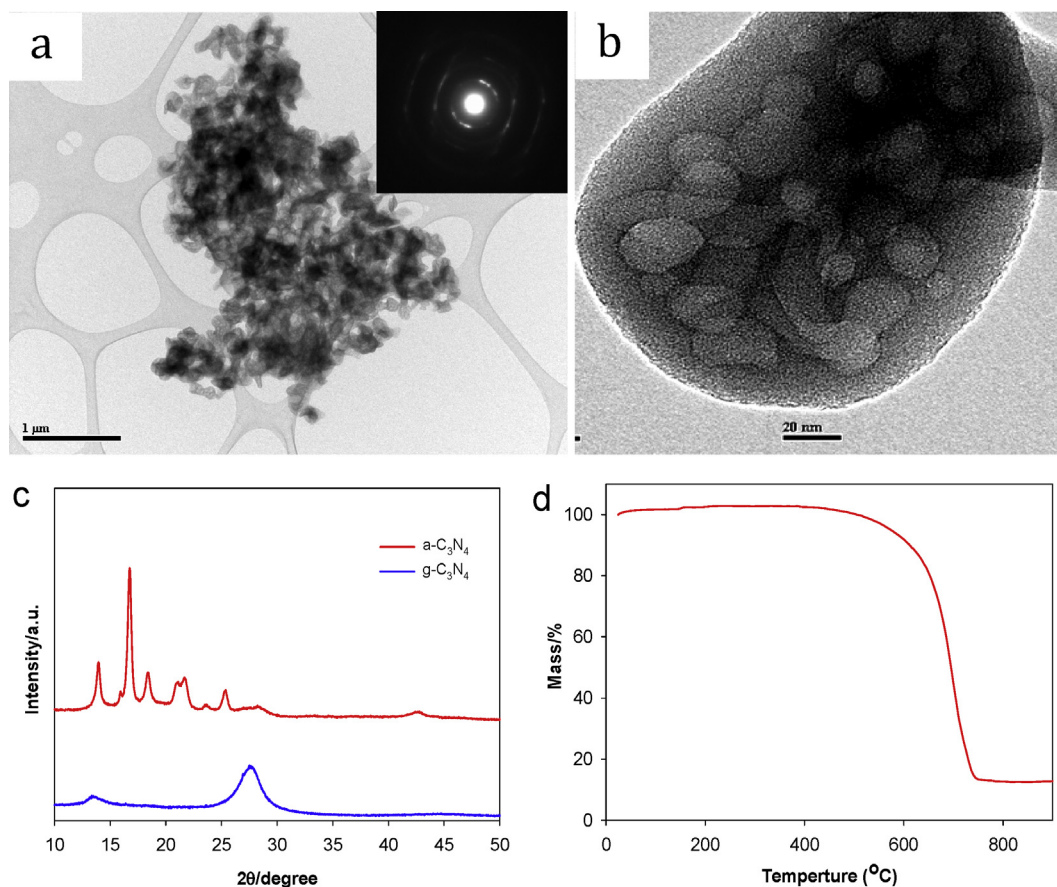


Fig. 1. Microstructure characterization and thermal analysis. (a) Low magnification TEM image of the synthesized nanoporous photocatalyst. Inset: the corresponding SAED pattern. (b) High magnification TEM image of the synthesized nanoporous photocatalyst. (c) XRD patterns of the nanoporous $\alpha\text{-C}_3\text{N}_4$ and $g\text{-C}_3\text{N}_4$ photocatalysts. (d) Thermogravimetric analysis curve of the synthesized $\alpha\text{-C}_3\text{N}_4$ sample.

429. The chemical composition of the nanoporous product was also analyzed using an elemental analyzer (Vario EL Cube).

Photocurrent measurements were carried out utilizing a three-electrode configuration with a Pt coil electrode as the counter electrode and a double junction saturated Ag/AgCl reference electrode, which was controlled by a PGZ 301 (Radiometer Analytical) potentiostat. The electrolyte consisted of a 0.5 M Na_2SO_4 solution, which was purged with argon to remove any dissolved oxygen prior to all experiments.

2.3. Photocatalytic activity tests

The photocatalytic activity of the synthesized nanoporous photocatalysts was evaluated by measuring the hydrogen evolution and the photodegradation of Rhodamine B (an organic dye pollutant) under visible light. All reactions were carried out in a Pyrex reaction vessel.

In a general experiment, 20 mg of the photocatalyst was suspended in 20 ml of an aqueous 25 μM RhB solution. The reaction mixture was sonicated for 30 min in the absence of light in order to obtain a homogeneous suspension having adsorption–desorption equilibrium. The light source used was an Oriel system that included a 300 W xenon arc lamp. For visible light irradiance, source light was passed through an optical filter (Edmund Optical Co.), which blocked wavelengths of below 420 nm. Infrared light was removed via a water filter. The intensity of the resulting visible light was $\sim 2.50 \text{ mW cm}^{-2}$. The temperature of the suspension and

its distance from the light source were kept constant. Samples were collected from the reaction mixture every 10 min to quantify the degradation of the RhB using a UV–vis spectrometer.

H_2 generation experiments were performed by dispersing 20 mg of the photocatalyst within an aqueous solution (10 mL) containing methanol (10 vol.%) as sacrificial electron donor and H_2PtCl_6 (1.5%). The reactant solutions were evacuated several times to remove oxygen completely prior to irradiation under a 300 W xenon arc lamp and a water filter. The reactant solution was maintained at room temperature by means of a flow of cooled water during the reaction. The evolved gases were analyzed by gas chromatography (GC-14B), which was equipped with a thermal conductive detector.

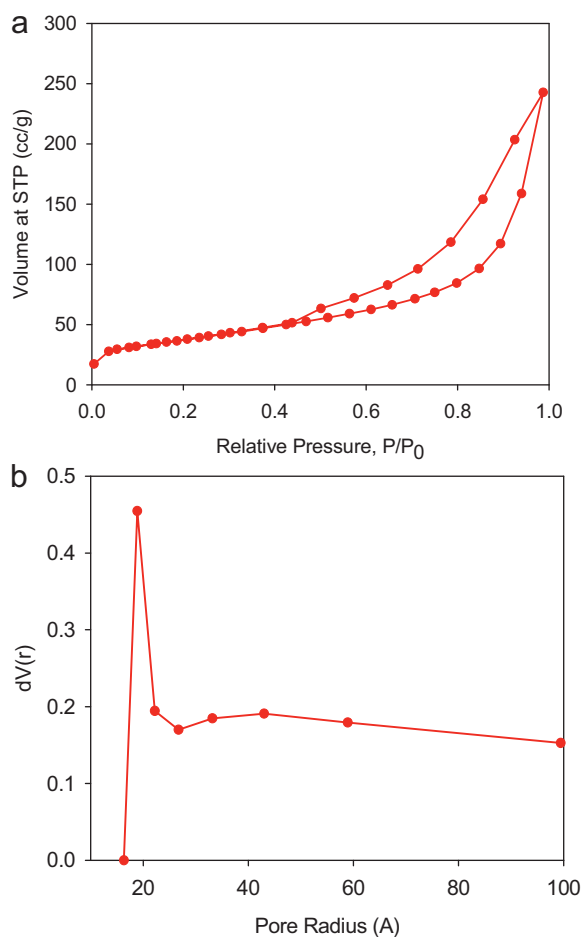


Fig. 2. (a) Nitrogen adsorption–desorption isotherm of the nanoporous $\alpha\text{-C}_3\text{N}_4$ sample after annealing at 450°C for 2 h. (b) Pore size distribution calculated from the adsorption branch of the isotherms.

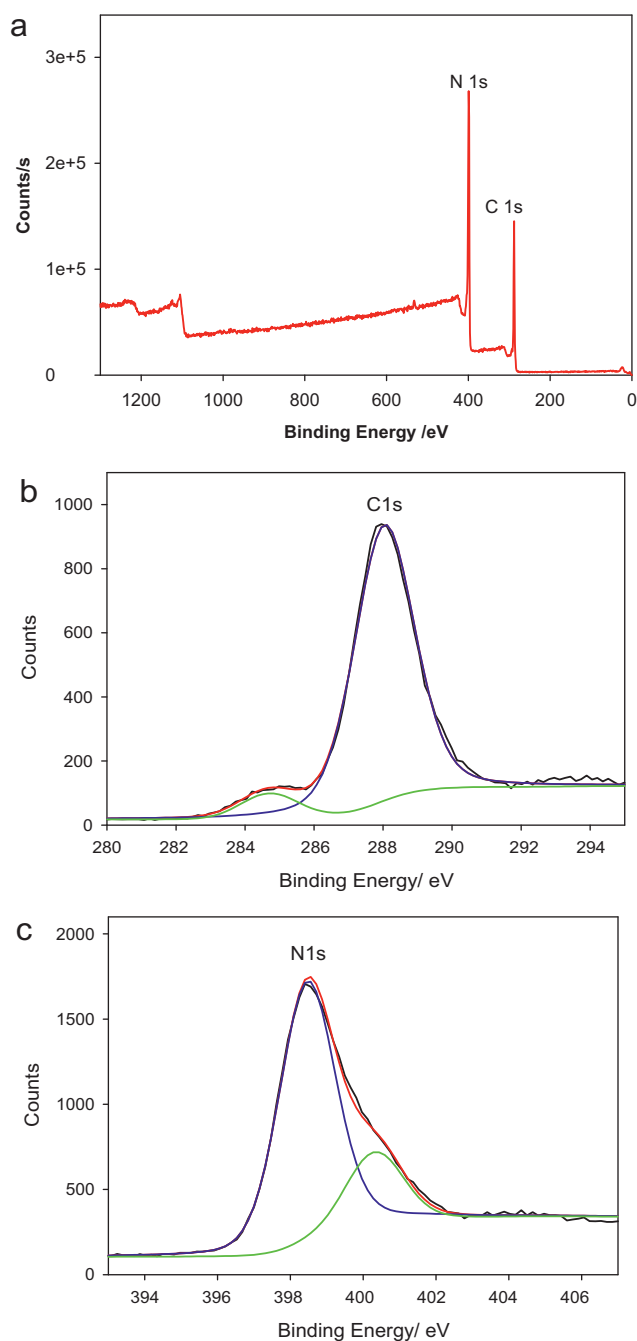


Fig. 3. (a) Survey scan XPS spectrum of the nanoporous $\alpha\text{-C}_3\text{N}_4$ sample. (b) High resolution XPS spectrum of C1s. (c) High resolution XPS spectrum of N1s.

3. Results and discussion

A typical low magnification TEM image of the obtained nanoporous α - C_3N_4 photocatalyst is presented in Fig. 1a; quite uniform pore structure in large area is observed, revealing that the product is homogenous. A high magnification TEM image is shown in Fig. 1b, depicting a uniform porous structure with a median pore size of ~ 2 nm. These nanopores were likely formed during the course of the solution combustion reaction, which released a large volume of gas-filled microbubbles. The dotted ring selected area electron diffraction (SAED) pattern (inset Fig. 1a) indicates that the as-prepared sample is polycrystalline in nature with a preferred grain orientation that corresponds to the interlayer d -spacing of α - C_3N_4 . Fig. 1c depicts the XRD patterns of the α - C_3N_4 photocatalyst. Several sharp peaks appeared in the range between 12° and 30° , which indicate high crystallinity of the as-synthesized samples. The strongest XRD peak at 16.7° may be indexed to the (1 0 0) plane of α - C_3N_4 . It is known that α - C_3N_4 is the most energetically

stable phase of all carbon nitride phases. As temperatures during the solution combustion reaction can attain several hundred degrees, it is reasonable to assume that the most stable phase will be obtained in this process. The XRD pattern of g- C_3N_4 prepared by annealing melamine is also shown in Fig. 1c for comparison. Two broad characteristic peaks attributed to g- C_3N_4 located at 13.6 ($1\ 0\ 0$) and 27.4 ($0\ 0\ 2$) can be observed; the strong peak at 27.4° which corresponds to 0.326 nm is due to the stacking of the conjugated aromatic system in graphite. This is consistent with values reported in the literature. No peaks corresponding to other phases are visible in this pattern.

Thermogravimetric analysis (TGA) was carried out in order to determine the thermal stability of the as synthesized α - C_3N_4 photocatalyst. As shown in Fig. 1d, when the temperature was increased from room temperature to 500°C , the photocatalyst was very stable and no obvious mass reduction was observed. A gradual loss in mass was observed, however, when the temperature was increased from 500 to 600°C , and a sharp mass diminution

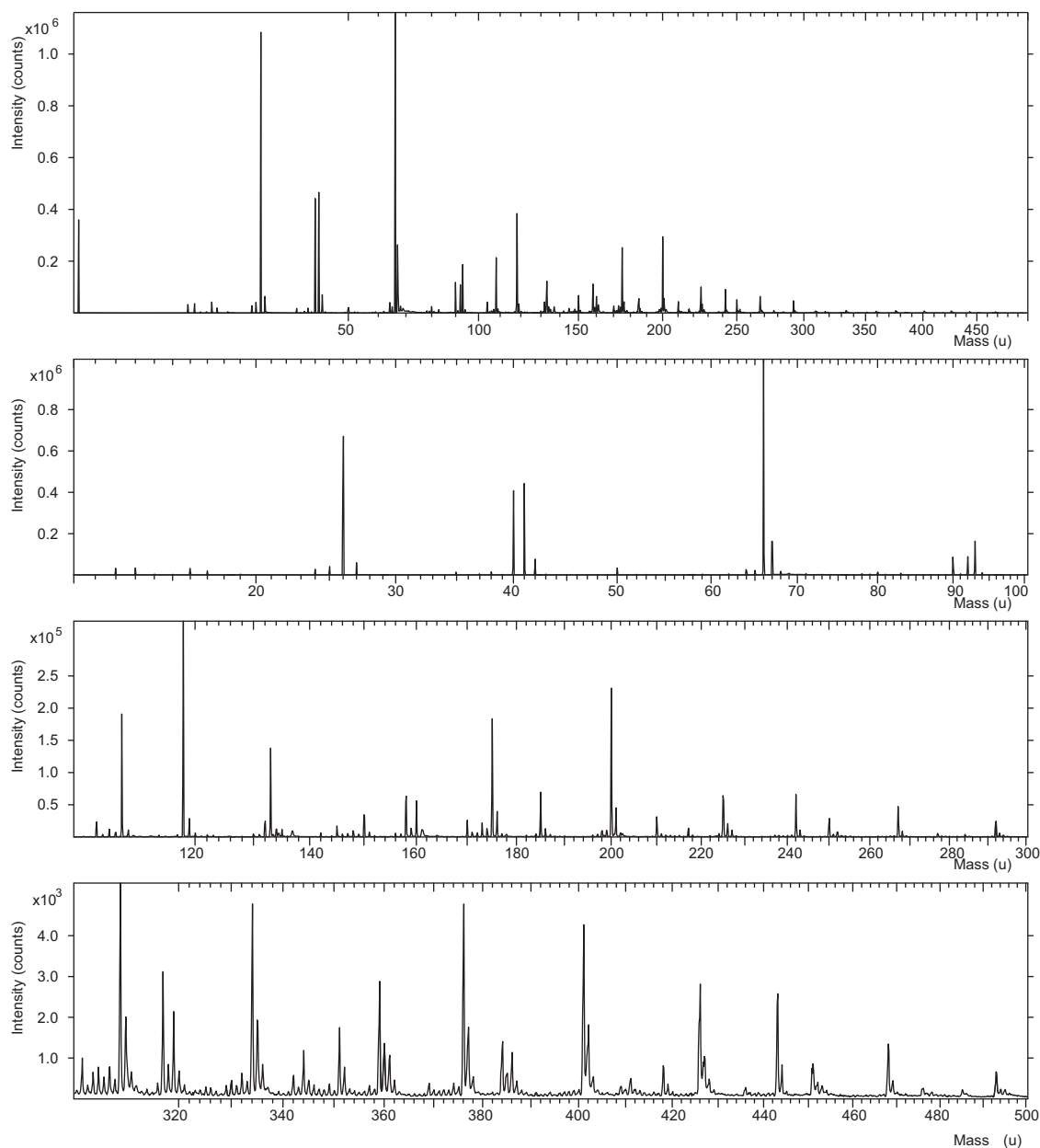


Fig. 4. SIMS spectrum of nanoporous α - C_3N_4 sample annealed at 450°C for 2 h.

occurred when the temperature was further elevated from 600 to 750 °C, where less than 15% of the original weight remained.

The nitrogen adsorption isotherm measured at 77 K with the sample that was annealed at 450 °C for 2 h is presented in Fig. 2a. The isotherm curve exhibited a type IV curve with a H hysteresis loop at a relative pressure in the range of 0.4–0.6, confirming the presence of pore structure. Brunauer–Emmett–Teller (BET) analysis revealed that the formed porous sample possessed a high specific surface area of 135.6 m²/g, which is over two-fold greater than that of Degussa P25 (55.4 m²/g), one of the best commercially available TiO₂ photocatalysts. This may be attributed to the diminutive particle size and the formed nanoporous structure, in good agreement with the TEM results as shown in Fig. 1a. The pore size distribution curve calculated from the desorption branch of the nitrogen isotherm via the BJH method using the Halsey equation is presented in Fig. 2b, indicating that the synthesized photocatalyst possesses a nanoporous structure with the majority of mesopore diameters at ~2.0 nm, whereas the minority of micropore diameters is ~0.11 nm based on the DA method. In the solution combustion reaction, urea served as both C and N source and fuel; the high temperature around 400 °C of the solution triggered the combustion reaction. As a result, large amount of heat was generated during the combustion reaction process and abundant tiny ammonia gas microbubbles were released into solution during the combustion reaction and remained to form the porous structure following the annealing process.

The composition of the nanoporous photocatalyst, which was annealed at 450 °C for 2 h, was further analyzed by XPS. As presented in Fig. 3a, two primary peaks attributed to C and N can be observed in the survey scan, where the atomic ratio of C and N is

~1.25. The two strong peaks were located at 288.0 and 398.4 eV, observed in the C 1s (Fig. 3b) and in the N 1s (Fig. 3c) XPS spectra, respectively. The C 1s spectrum can be deconvoluted into two peaks that are associated with different binding energies. The C 1s peak at 288.0 eV may be assigned to the sp³-type C–N bonds; the peak at 284.5 eV originates from the simultaneous contribution of C–C bonding in graphite and adventitious carbon [37]. The N 1s band of the XPS spectrum can be deconvoluted in two individual peaks, at 398.4 and 400.3 eV, respectively. The nitrogen peaks could be attributed to tetrahedral sp³ bonding and sp² CN bonding, respectively. The XPS measurements show the existence of a carbon–nitrogen single-banded configuration of the type expected in α - or β -C₃N₄ structures [38]. Other bonding configurations such as C=N, also seem to be present, which might be assigned to g-C₃N₄. Considering the very weak peak at 27.4° in the XRD pattern (Fig. 1c), which is the characteristic peak due to the stacking of the conjugated aromatic system (as in graphite), it can be concluded that there is only a small amount of g-C₃N₄ that exists in the product.

The corresponding ToF-SIMS spectra are shown in Fig. 4. In the fingerprint region, the fragments at *m/z* 26, 40, 66 can be assigned to CN, CN₂ and C₂N₃ groups, respectively, indicating that the as-synthesized photocatalyst has a repeating C–N unit backbone. In the high *m/z* region, the fragments may be assigned to variable CN chain lengths. Elemental analysis of the synthesized nanoporous sample was also conducted. The result showed that the atomic ratio of C to N is ~1.4, which is very close to the ratio calculated from XPS data. All of these results are consistent with XRD and ToF-SIMS analyses, which further confirm that the prepared novel nanoporous sample was α -C₃N₄.

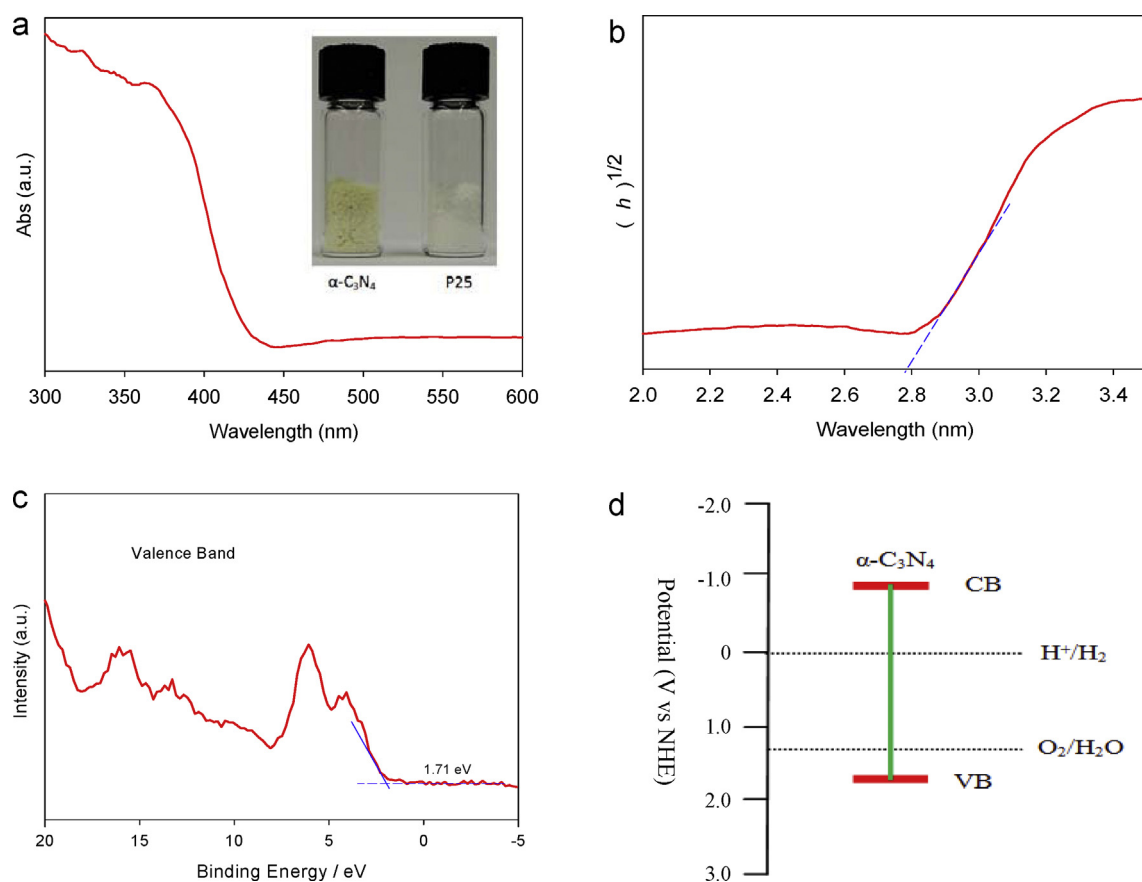


Fig. 5. Optical properties characterization and band gap. (a) UV–vis absorption spectrum of the nanoporous photocatalyst subsequent to annealing at 450 °C for 2 h, (inset: photos of P25 and the synthesized nanoporous α -C₃N₄ sample). (b) The corresponding Tauc plot shown in (a). (c) Valence band XPS spectrum of the nanoporous photocatalyst. (d) Schematic energy diagram of the novel nanostructured photocatalyst with respect to water splitting.

A UV–vis spectrum of the nanoporous photocatalyst is presented in Fig. 5a. As seen in the inset of Fig. 5a, the photocatalyst is yellow and has a strong visible light absorption. The Tauc plots, $(\alpha h\nu)^{1/2}$ vs. $h\nu$, obtained after substituting the value of α , is presented in Fig. 5b. The optical band gap, estimated by drawing a line from the maximum slope of the curve to the x-axis is 2.76 eV, which is much smaller than that of P25 (3.20 eV). In order to understand the band position, a valence band XPS measurement was also conducted. Based on the valence band XPS spectrum as shown in Fig. 5c, the conduction band gap of this nanoporous photocatalyst was estimated to be 1.02 eV. Fig. 5d depicts a schematic diagram of the relative position of valence and conduction band gap energies with respect to the electrode potential of the two half-reactions of the water splitting process. This is unprecedented, not only because the narrow band gap energy takes advantage of visible light, but also the absolute energies of valence and conduction band gaps with respect to water reduction and oxidation levels, which make this photocatalyst ideal for water splitting.

In order to evaluate the visible light response of the nanoporous materials, a photoelectrochemical test was conducted. Fig. 6 shows the time course for the photocurrent response of the porous α - C_3N_4 photocatalyst at a fixed potential of 0.6 V vs. Ag/AgCl in a 0.5 M Na_2SO_4 solution under continuous visible light irradiation ($\lambda > 420$ nm). This indicates that the photocatalyst is an n-type semiconductor and shows a very high visible light response; the photocurrent density can attain $25 \mu\text{A}/\text{cm}^2$ at 0.6 V due to the high surface area, low band gap energy and high crystallinity of the photocatalyst. The photocurrent of the g- C_3N_4 electrode under the same conditions is also shown in Fig. 6 for comparison. It can be

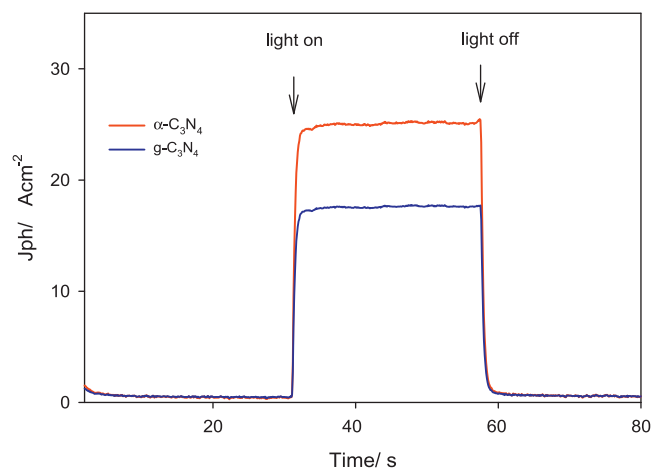


Fig. 6. Time courses of the photocurrent of nanoporous photocatalyst g- C_3N_4 and α - C_3N_4 in 0.5 M Na_2SO_4 under visible light irradiation at 0.6 V vs. Ag/AgCl.

seen that the photocurrent is $\sim 18 \mu\text{A}/\text{cm}^2$ at 0.6 V, which is $\sim 30\%$ lower than that of α - C_3N_4 , indicating that α - C_3N_4 has the capacity for harvesting and separating charge more efficiently than g- C_3N_4 . This also signifies that the α - C_3N_4 has higher quantum efficiency than g- C_3N_4 .

In order to examine the photocatalytic performance of the nanoporous photocatalyst, the photodegradation of Rhodamine B (RhB) under visible light ($\lambda > 420$) was evaluated and compared

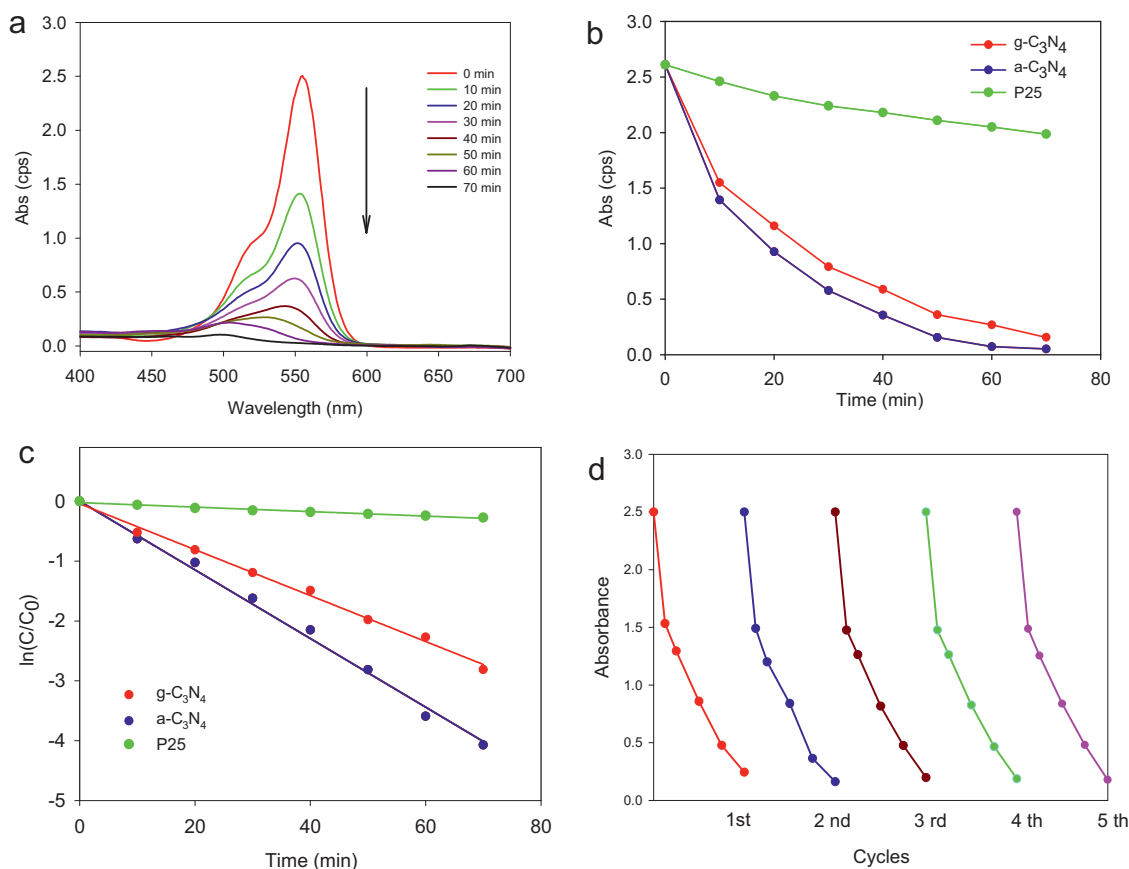


Fig. 7. Photocatalytic activity tests. (a) Typical UV–vis spectra of RhB obtained during the photodegradation of 0.025 mM Rhodamine B solution in the presence of the nanoporous photocatalyst under visible light. (b) RhB degradation in the presence of P25, g- C_3N_4 and α - C_3N_4 under visible-light. (c) Kinetic curves for the photodegradation of Rhodamine B over P25, g- C_3N_4 and α - C_3N_4 . (d) Stability cycling experiments of the photocatalytic degradation of RhB using the nanostructured α - C_3N_4 photocatalyst under visible light irradiation.

with Degussa P25 and $g\text{-C}_3\text{N}_4$. Fig. 7a presents the absorption curve, illustrating the course of RhB degradation over different time periods in the presence of the nanoporous photocatalyst. A comparison of the photodegradation of the dye on P25, $g\text{-C}_3\text{N}_4$ and the as-synthesized photocatalyst samples, are presented in Fig. 7b. Kinetic calculations revealed that the ratio of the photodegradation of RhB on the polymeric sample is much higher than P25 (Fig. 7c), indicating a significant enhancement in visible light induced photocatalytic activity. It can also be seen that the photocatalytic activity of $\alpha\text{-C}_3\text{N}_4$ is higher than that of $g\text{-C}_3\text{N}_4$, even though they can both absorb visible light. We further tested the stability of this unique photocatalyst. The cycling test results of its visible light photocatalytic activity in the decomposition of RhB are presented in Fig. 7d. Once the photocatalytic reaction of a testing cycle was completed, the solution was centrifuged and the photocatalyst was dried. A subsequent cycle was initiated following the addition of the original RhB solution. No reduction in photocatalytic activity was observed in the cycling tests, demonstrating that this new photocatalyst possessed high photochemical stability under long duration irradiation.

The nanoporous $\alpha\text{-C}_3\text{N}_4$ photocatalyst was tested further in terms of H_2 generation. Fig. 8 illustrates the time course of H_2 generation on the $\alpha\text{-C}_3\text{N}_4$, $g\text{-C}_3\text{N}_4$ and P25 photocatalysts as aqueous suspensions under visible light ($\lambda > 420\text{ nm}$) irradiation. As expected, the generation of H_2 from P25 under visible light was negligible (Fig. 8); both $g\text{-C}_3\text{N}_4$ and $\alpha\text{-C}_3\text{N}_4$ showed strong visible light activity in terms of H_2 generation, which is due to their small band gap energy for harvesting a broad range of wavelengths from the light source, and proper band edge alignment with respect to water splitting. As shown in Fig. 8, the hydrogen evolution rate over the $g\text{-C}_3\text{N}_4$ photocatalyst was $\sim 0.8\ \mu\text{mol h}^{-1}$, whereas H_2 generation over $\alpha\text{-C}_3\text{N}_4$ was $\sim 1.4\ \mu\text{mol h}^{-1}$, which is much higher than that of $g\text{-C}_3\text{N}_4$. Since both $g\text{-C}_3\text{N}_4$ and $\alpha\text{-C}_3\text{N}_4$ have similar band gap energies, the chief difference with respect to hydrogen evolution over $g\text{-C}_3\text{N}_4$ and $\alpha\text{-C}_3\text{N}_4$ might be attributed to different crystal structures and degrees of crystallinity. As we can see from Fig. 1b, $\alpha\text{-C}_3\text{N}_4$ exhibited sharper peaks in the XRD pattern, indicating that it contains a lower concentration of defects, which might serve as charge recombination centers. This assumption may also be validated by the photocurrent response of $g\text{-C}_3\text{N}_4$ and $\alpha\text{-C}_3\text{N}_4$ under visible light irradiation, as is illustrated in Fig. 6.

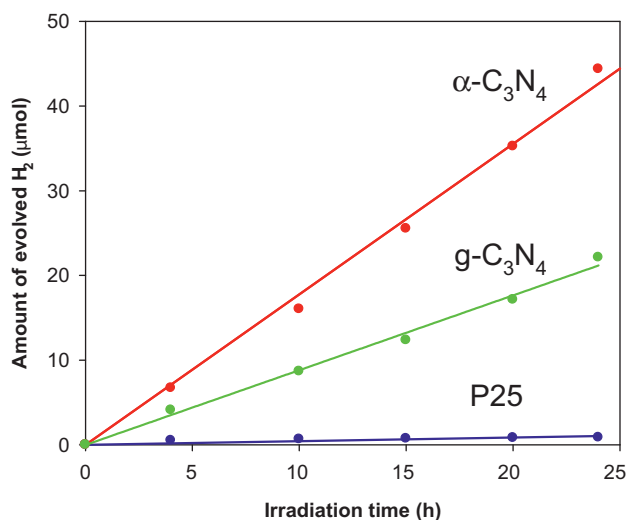


Fig. 8. H_2 production over different photocatalysts. Variation of the amount of H_2 generated vs. time on the $\alpha\text{-C}_3\text{N}_4$, $g\text{-C}_3\text{N}_4$ and P25 photocatalyst under visible light irradiation.

4. Conclusions

In summary, we have developed a novel non-metal $\alpha\text{-C}_3\text{N}_4$ nanoporous photocatalyst that was successfully synthesized via an inexpensive urea precursor using a rapid and facile solution combustion process. Structural analysis has shown that the new photocatalyst is a CN chain based nanomaterial with high surface area, crystallinity and thermal stability. It not only harvests visible light by virtue of its low band gap energy ($\sim 2.76\text{ eV}$), but also possesses ideal valence and conduction band edge alignment in terms of H_2 production from water splitting. Our experimental results also show that this novel photocatalyst has higher photocatalytic activity in terms of decomposition of RhB and water splitting due to its high quantum efficiency. Hence, the new robust $\alpha\text{-C}_3\text{N}_4$ photocatalyst reported in this study holds unprecedented potential in addressing critical environmental and energy issues.

Acknowledgments

This work was supported by a Discovery Grant from the Natural Sciences and Engineering Research Council of Canada (NSERC). A.C. acknowledges NSERC and the Canada Foundation of Innovation (CFI) for the Canada Research Chair Award in Materials and Environmental Chemistry.

References

- [1] N.Z. Muradov, T.N. Veziroglu, *Int. J. Hydrogen Energy* 33 (2008) 6804.
- [2] B. Adams, A. Chen, *Mater. Today* 14 (2011) 282.
- [3] R.M. Navarro, M.A. Pena, J.L.G. Fierro, *Chem. Rev.* 107 (2007) 3952.
- [4] M.G. Walter, E.L. Warren, J.R. McKone, S.W. Boettcher, Q.X. Mi, E.A. Santori, N.S. Lewis, *Chem. Rev.* 111 (2011) 5815.
- [5] F. Amamo, O. Prieto-Mahaney, Y. Terada, T. Yasumoto, T. Shibayama, B. Ohtani, *Chem. Mater.* 21 (2009) 2601–2603.
- [6] Z.G. Zou, J.H. Ye, K. Sayama, H. Arakawa, *Nature* 414 (2001) 625.
- [7] J. Zhang, J.G. Yu, Y.M. Zhang, Q. Li, J.R. Gong, *Nano Lett.* 11 (2011) 4774.
- [8] J.W. Sun, C. Liu, P.D. Yang, *J. Am. Chem. Soc.* 133 (2011) 19306.
- [9] S.Y. Reece, J.A. Hamel, K. Sung, T.D. Jarvi, A.J. Esswein, J.H. Pijpers, D.G. Nocera, *Science* 334 (2011) 645.
- [10] M. Liu, X.Q. Qiu, M. Miyauchi, K. Hashimoto, *Chem. Mater.* 23 (2011) 5282–5286.
- [11] D. Lehr, M. Luka, M.R. Wagner, M. Bugler, A. Hoffmann, S. Polarz, *Chem. Mater.* 24 (2012) 1771–1778.
- [12] Y.J. Lin, G.B. Yuan, S. Sheehan, S. Zhou, D.W. Wang, *Energy Environ. Sci.* 4 (2011) 4862.
- [13] N.D. Petkovich, S.G. Rudisill, L.J. Venstrom, D.B. Boman, J.H. Davidson, A. Stein, *J. Phys. Chem. C* 115 (2011) 21022.
- [14] A. Thibert, F.A. Frame, E. Busby, M.A. Holmes, F.E. Osterloh, D.S. Larsen, *J. Phys. Chem. Lett.* 2 (2011) 2688.
- [15] K. Iwashina, A. Kudo, *J. Am. Chem. Soc.* 133 (2011) 13272.
- [16] S.U.M. Khan, M. Al-Shahry, W.B. Ingler, *Science* 297 (2002) 2243.
- [17] S.S. Thind, G. Wu, M. Tian, A. Chen, *Nanotechnology* 23 (2012) 475706.
- [18] G. Wu, T. Nishikawa, B. Ohtani, A. Chen, *Chem. Mater.* 19 (2007) 4530–4537.
- [19] S.S. Thind, G. Wu, A. Chen, *Appl. Catal. B: Environ.* 111 (2012) 38–45.
- [20] N. Govind, K. Lopata, R. Rousseau, A. Andersen, K. Kowalski, *J. Phys. Chem. Lett.* 2 (2011) 2696.
- [21] M.Y. Xing, D.Y. Qi, J.L. Zhang, F. Chen, *Chem. – Eur. J.* 17 (2011) 11432.
- [22] V. Stengl, J. Velicka, M. Marikova, T. Matys Grygar, *ACS Appl. Mater. Interfaces* 3 (2011) 4014.
- [23] A. Mattsson, M. Leideborg, K. Larsson, G. Westin, L. Osterlund, *J. Phys. Chem. B* 110 (2006) 1210.
- [24] G.S. Wu, J.P. Wang, D.F. Thomas, A.C. Chen, *Langmuir* 24 (2008) 3503.
- [25] Y.G. Zhang, L.L. Ma, J.L. Li, Y. Yu, *Environ. Sci. Technol.* 41 (2007) 6264.
- [26] S. Mubeen, G. Hernandez-Sosa, D. Moses, J. Lee, M. Moskovits, *Nano Lett.* 11 (2011) 5548.
- [27] G. Wu, M. Tian, A. Chen, *J. Photochem. Photobiol. A: Chem.* 233 (2012) 65–71.
- [28] T. Lopez-Luke, A. Wolcott, L.P. Xu, S.W. Chen, Z.H. Wen, J.H. Li, E. Rosa De La, J.Z. Zhang, *J. Phys. Chem. C* 112 (2008) 1282.
- [29] A. Kongkanand, K. Tvrđy, K. Takechi, M. Kuno, P.V. Kamat, *J. Am. Chem. Soc.* 130 (2008) 4007.
- [30] G. Liu, Y.N. Zhao, C.H. Sun, F. Li, G.Q. Lu, H.M. Cheng, *Angew. Chem. – Int. Ed.* 47 (2008) 4516.
- [31] X.C. Wang, K. Maeda, A. Thomas, K. Takanabe, G. Xin, J.M. Carlsson, K. Domen, M. Antonietti, *Nat. Mater.* 8 (2009) 76.

- [32] X.H. Li, J.S. Zhang, X.F. Chen, A. Fischer, A. Thomas, M. Antonietti, X.C. Wang, *Chem. Mater.* 23 (2011) 4344–4348.
- [33] A. Thomas, A. Fischer, F. Goettmann, M. Antonietti, J.O. Muller, R. Schlögl, J.M. Carlsson, *J. Mater. Chem.* 18 (2008) 4893–4908.
- [34] Z.J. Huang, F.B. Li, B.F. Chen, T. Lu, Y. Yuan, G.Q. Yuan, *Appl. Catal. B: Environ.* 136–137 (2013) 269–277.
- [35] L. Ge, C.C. Han, *Appl. Catal. B: Environ.* 117–118 (2012) 268–274.
- [36] T.T. Li, L.H. Zhao, Y.M. He, J. Cai, M.F. Luo, J.J. Lin, *Appl. Catal. B: Environ.* 129 (2013) 255–263.
- [37] Y.G. Li, J. Zhang, Q.S. Wang, Y.X. Jin, D.H. Huang, Q.L. Cui, G.T. Zou, *J. Phys. Chem. B* 114 (2010) 9429.
- [38] S. Kundu, W. Xia, W. Busser, M. Becker, D.A. Schmidt, M. Havenith, M. Muhler, *Phys. Chem. Chem. Phys.* 12 (2010) 4351.